Nanoscale

PAPER

Cite this: *Nanoscale*, 2016, **8**, 7180

A comprehensive study on atomic layer deposition of molybdenum sulfide for electrochemical hydrogen evolution†

Do Hyun Kwon,‡[a,b] Zhenyu Jin,‡[a] Seokhee Shin,[a] Wook-Seong Lee*[b] and Yo-Sep Min*[a]

Received 21st December 2015,
Accepted 23rd February 2016

DOI: 10.1039/c5nr09065b

www.rsc.org/nanoscale

Atomic layer deposition (ALD) has emerged as an efficient method to design and prepare catalysts with atomic precision. Here, we report a comprehensive study on ALD of molybdenum sulfide (MoS_x) for an electrocatalytic hydrogen evolution reaction. By using molybdenum hexacarbonyl and dimethyldisulfide as the precursors of Mo and S, respectively, the MoS_x catalysts are grown at 100 °C on porous carbon fiber papers (CFPs). The ALD process results in the growth of particle-like MoS_x on the CFP due to the lack of adsorption sites, and its crystallographic structure is a mixture of amorphous and nano-crystalline phases. In order to unveil the intrinsic activity of the ALD-MoS_x, the exchange current densities, Tafel slopes, and turnover frequencies of the catalysts grown under various ALD conditions have been investigated by considering the fractional surface coverage of MoS_x on the CFP and catalytically-active surface area. In addition, the ALD-MoS_x/CFP catalysts exhibit excellent catalytic stability due to the strong adhesion of MoS_x on the CFP and the mixed phase.

1 Introduction

Over the past few decades, researchers have studied a variety of renewable energy sources in order to find a sustainable alternative to conventional hydrocarbon fuel. Hydrogen gas is one of the most environmentally friendly fuels with large energy density. However, for the hydrogen fuel to become a viable alternative to hydrocarbon fuels, it must be produced in a sustainable manner. The electrochemical hydrogen evolution reaction (HER) has been considered as one of the most important pathways to efficiently produce hydrogen fuel without carbon dioxide emissions.[1] The highly efficient HER catalysts mainly consist of rare elements such as platinum group metals which are very expensive due to their low abundance on the earth.[2,3] Therefore, many researchers are actively searching for alternative catalysts consisting of low-cost elements.[4]

Recently, molybdenum disulfide (MoS_2) has attracted great attention due to its biomimetic hydrogen evolving activity.[5,6] However, MoS_2 has a poor activity for the HER in its bulk form,[7] because the active sites of MoS_2 are located at the edge sites and not at the basal planes.[8] Thus, the catalytic surface of the crystalline MoS_2 needs to be engineered in order to increase the number of the active edge sites in the geometrical area of the catalyst. There are many reports on the improved HER activity of MoS_2 by the edge-site engineering: MoS_2 nanoparticles on reduced graphene oxide,[9] core–shell MoS_2 nanowire,[10] double-gyroid MoS_2 template,[11] MoS_2 on mesoporous carbon,[12] vertically-aligned MoS_2,[13] and so on.[14,15]

Recently, it is also reported that the amorphous phase of molybdenum sulfide (MoS_x) exhibits a high HER activity, because of its abundant active sites on the surface.[16,17] The electrocatalytic activity of the amorphous MoS_x has been explored by using various synthesis methods such as electrochemical deposition, wet chemical synthesis and hydrothermal growth.[16–19]

In our previous work, we have reported that amorphous MoS_2 thin films could be grown by atomic layer deposition (ALD) owing to the low growth temperature of 100 °C, in which molybdenum hexacarbonyl [$Mo(CO)_6$] and dimethyldisulfide [DMDS ($CH_3S_2CH_3$)] were used as the precursors of Mo and S, respectively.[20] Recently, we have also demonstrated that the amorphous MoS_2 grown on a Au/Ti/Si substrate by ALD effectively catalyses the HER with a high turnover frequency of 3 H_2 per s at an overpotential of 0.215 V.[21] In addition, the ALD-MoS_2 has a high conductivity of 0.22 Ω^{-1} cm^{-1} at room temperature, which contributes to the excellent HER activity.

[a]*Department of Chemical Engineering, Konkuk University, 120 Neungdong-Ro, Gwangjin-Gu, Seoul 143-701, Korea. E-mail: ysmin@konkuk.ac.kr*
[b]*Electronic Materials Center, Korea Institute of Science and Technology, Seongbuk-Gu, Seoul 136-791, Korea. E-mail: wsleemk@gmail.com*

†Electronic supplementary information (ESI) available: Nyquist plots, cyclic voltammograms, STEM-EDS images, Raman spectra of MoS_x/CFP catalysts. See DOI: 10.1039/c5nr09065b

‡These authors equally contributed to this work.

The ALD method is an efficient tool to design and prepare catalysts with atomic scale precision.[22] Because the catalysts grow *via* self-limiting chemisorptions of the precursor molecules, the thickness or amount of the catalyst can be controlled with a great precision by changing the number of ALD cycles. On the other hand, to increase the performance of the electrocatalyst, the area of the catalytic surface can be increased by using a porous conductor as a supporting substrate on which the electrocatalyst grows. It is possible to prepare MoS_x catalysts on highly porous substrates by using the conformal growth behavior of the ALD process. When porous substrates are used as the supporting substrate, the ALD method is very useful, due to its ability to deposit the catalyst onto the entire surface of both the interior and the exterior of the supporting material. Regardless of the structure and shape of the porous substrate, ALD can grow a conformal film on the porous substrate, due to the self-limiting growth mechanism of ALD *via* chemical adsorption of precursors.[23]

The conformal coating of the catalyst on porous substrates by the ALD method is a great way to increase the number of active sites, and several groups have utilized the ALD process to prepare HER catalysts. Yang *et al.* demonstrated ALD of Pt catalysts on the surface of Si/TiO_2 core–shell nanowires for photoelectrochemical water reduction.[24] Cui *et al.* prepared a vertically aligned MoS_2 catalyst by sulfurizing the ALD-grown MoO_3 thin film.[13] However, there is no comprehensive study on the ALD of MoS_2 directly grown on porous substrates. Furthermore, although the ALD-MoS_2 catalyst on the flat Au substrate has shown excellent activity (Tafel slope: 47 mV dec^{-1}, exchange current density: $\sim 10^{-8}$ mA cm^{-2}), the catalytic activity of the ALD-MoS_2 is not stable due to its weak adhesion.[21] Therefore, it is necessary to replace the supporting Au substrate with a cheap and porous substrate, which can provide a large electrochemically-active surface area and can strengthen the adhesion of the amorphous MoS_2.[25] In this work, carbon fiber papers (CFPs) are chosen as the supporting substrate to utilize its large specific surface area. We investigate the ALD behavior of the molybdenum sulfide on the CFP to precisely design and prepare the electrocatalyst with high HER activity and stability. We discuss several factors such as crystallinity, fractional surface coverage and catalytically active surface area of the catalyst in order to unveil their influence on catalytic performance.

2 Experimental

In order to investigate the ALD behavior of molybdenum sulfide, MoS_x thin films were simultaneously grown on both CFP (2×2 cm^2, Toray, TGP-H-120) and bare Si (2×2 cm^2) substrates at 100 °C in a laminar flow type ALD reactor. The films grown on the dummy Si substrates were used to estimate the thickness of MoS_x. $Mo(CO)_6$ and dimethyldisulfide (DMDS) were vaporized from external canisters at room temperature and led into the reactor through solenoid valves with N_2 as a carrier gas (100 sccm, 99.999%) for $Mo(CO)_6$ and without carrier gas for DMDS. The doses of $Mo(CO)_6$ and DMDS were $\sim 1.8 \times 10^{-6}$ and $\sim 4.0 \times 10^{-4}$ mol s^{-1}, respectively. For purging the reactor, N_2 gas was used with a flow rate of 300 sccm. All delivery lines were maintained at 80 °C.

The thicknesses of MoS_x were measured on the films grown on the bare Si by using a spectroscopic ellipsometer (SE, MG-1000, NanoView) with a spectral range of 1.5–5.0 eV. The incident angle of the polarized light in the SE was fixed at around 70°. The measured data by SE were fitted with a Tauc–Lorentz dispersion function to determine the thickness. X-ray photoelectron spectroscopy (XPS) spectra were obtained on a PHI 5000 Versaprobe (ULVAC PHI) using monochromatic Al Kα emission. Binding energies were calibrated by using the carbon 1s peak at 284.8 eV. For transmission electron microscopy (TEM) analyses, the carbon fibers were detached from the MoS_x/CFP sample, and their microstructures were imaged in a TITAN TM 80-300 FEI microscope. Scanning electron microscopy (SEM) and energy-dispersive spectroscopy (EDS) images were obtained by using a scanning electron microscope (JEOL JSM-6380) with an EDS detector (Oxford Instruments, INCA X-act). X-ray diffraction (XRD) patterns were recorded using a Philips X'pert Pro MRD X-ray diffractometer with Cu Kα emission. Raman spectra were obtained on a Raman spectrometer (Alpha 500R, WiTec) using a 532 nm laser excitation, after calibrating Raman shifts with Si as a reference at 521 cm^{-1}. The specific surface area of the CFP was measured by N_2 adsorption–desorption isotherms at 77 K using a Brunauer–Emmett–Teller (BET) surface analyser (Micrometrics, Tristar II 3020). The CFP samples were degassed at 120 °C for 12 h prior to the BET measurements, which were performed 3 times for three pieces of the CFP to obtain the mean value of the specific surface area.

The HER measurements were performed in 100 ml of 0.5 M H_2SO_4 electrolyte solution using a standard three-electrode cell with a Bio-Logic potentiostat (SP150). Saturated Hg/Hg_2SO_4, a graphite rod, and the MoS_x-coated CFP were used as the reference, counter, and working electrodes, respectively. For the preparation of the working electrode, the geometric area (A_g) of the MoS_x-coated CFP was defined to be 1 cm^2 with Kapton tape (see the ESI of ref. 21). The reference electrode was calibrated with respect to the reversible hydrogen electrode (RHE) by using two platinum wires as the working and counter electrodes in the 0.5 M H_2SO_4 solution, while purging 99.999% H_2 gas through the solution. The calibration gives an electrochemical potential (E) relationship between the RHE and counter electrode, E (RHE) = E (Hg/Hg_2SO_4) + 0.700 V. The polarization curves for the HER were obtained by linear sweep voltammetry (LSV) beginning at +0.1 V and ending at−0.30 V *vs.* RHE with a scan rate of 5 mV s^{-1}. In order to determine the series resistance of the electrochemical cell before each LSV experiment, electrochemical impedance measurement was performed at an open circuit potential from 200 kHz to 50 MHz, using an ac amplitude of 25 mV. The values of series resistance for each sample were in the range of 1–2 ohm. All the polarization curves were corrected for ohmic potential drop (iR) losses using the series resistance (see Fig. S1†). To estimate

the electrochemically active surface area (A_e) of the MoS_x-coated CFP, the double layer capacitance (C_{dl}) of the defined area (1 cm^2) was determined from cyclic voltammograms (see Fig. S2 and S3†) in a potential range of 0.1 to 0.2 V *vs.* RHE which were taken with various scan rates (20, 40, 60, 80, 100 V s^{-1}). The stability test was performed by repeating cyclic voltammetry for 1000 cycles from +0.1 V to −0.25 V *vs.* RHE at a scan rate of 50 mV s^{-1}.

3 Results and discussion

As shown in the schematic diagram in Fig. 1, molybdenum sulfide (MoS_x) is directly grown on the CFP at 100 °C by ALD from $Mo(CO)_6$ and DMDS. The CFP used in this work is a porous mat of crystalline carbon fibers whose average diameter is ~8 μm, and the thickness of the CFP is ~400 μm.[26] The specific surface area of the CFPs was estimated to be 0.384 m^2 g^{-1} (±0.145 m^2 g^{-1}) by the BET analysis. Because the mass of the CFP, whose geometric area (A_g) is 1 cm^2, is around 0.0187 g, the BET surface area (A_{BET}) of the CFP is *ca.* 70 times larger than the A_g value, owing to its porous structure. Here we define the ratio of A_{BET}/A_g as an area multiplication factor (k), *i.e.*, $k \sim 70$ for the CFP.

Even though the CFP is hydrophobic, the MoS_x was grown without any pretreatment process, because the growth occurs *via* the chemical adsorption of precursors in a vacuum.[19] Two sets of experiments were performed to investigate the ALD behavior. In the first set (A), the step times in the ALD sequence of $Mo(CO)_6$ exposure (M)–N_2 purging (P)–DMDS exposure (D)–N_2 purging (P) steps were set to be 4 s–30 s–1.5 s–30 s, while the number of cycles (N_{ALD}) was changed to 20, 60, 100, and 150. In the second experiment (B), the $Mo(CO)_6$ exposure time (x) was set to be 1, 4, 10, or 20 s in the sequence of M (x)–P (90 s)–D (3 s)–P (60 s) for N_{ALD} = 50 cycles.

The growth of MoS_x was monitored on both the dummy Si and the CFP substrates, which were simultaneously loaded in the ALD reactor, by measuring its thickness and electrical double layer capacitance (C_{dl}), respectively. Generally, the C_{dl} value is proportional to the electrochemically active surface area (A_e). The C_{dl} value of the bare CFP was measured to be $C_{dl}^{CFP} = C_{dl}^{\theta=0} \approx 7.9$ μF cm^{-2}, where θ is the fractional surface coverage of MoS_x on the CFP.[19] It is well known that the C_{dl} of MoS_2 is ~60 μF cm^{-2} in the form of a flat thin film.[17,27] Therefore, if molybdenum sulfide is completely grown with a uniform thickness on the entire surface of the CFP, the double layer capacitance ($C_{dl}^{MoS_x/CFP}$) of the MoS_x/CFP may reach $C_{dl}^{MoS_x/CFP} = C_{dl}^{\theta=1} \approx 4.2$ mF cm^{-2} which is 70 times larger than 60 μF cm^{-2}. Because of the large difference between $C_{dl}^{\theta=0}$ and $C_{dl}^{\theta=1}$, as the fractional surface coverage (θ) of MoS_x increases on the CFP during the early stages of the ALD cycles, the measured C_{dl} may rapidly increase to 4.2 mF cm^{-2} within several ALD cycles, following eqn (1),

$$C_{dl} = R_f C_{dl}^{\theta=1}\theta + C_{dl}^{\theta=0}(1-\theta) \approx R_f C_{dl}^{\theta=1}\theta \quad (1)$$

where R_f is a surface roughness factor defined as a ratio of the real surface area of MoS_x to the area of MoS_x projected onto the substrate. In the ideal case of ALD, $R_f \sim 1$. In addition, when θ is small, the approximate equation, $C_{dl} \approx R_f C_{dl}^{\theta=1}\theta$, is not valid, because the contribution of the second term is not negligible.

In Fig. 2a, the thickness of MoS_x on the Si substrate linearly increases as the ALD cycles are repeated. The growth-per-cycle (GPC) is evaluated to be 0.092 nm per cycle from the slope. Therefore, considering the GPC and the density (2.9 g cm^{-3}) of the amorphous ALD-MoS_2 thin film, the complete coverage of MoS_2 can be achieved within 5 cycles under the assumption of conformal and uniform growth on the CFP. However, the C_{dl} values in Fig. 2a are much smaller than the expected value of

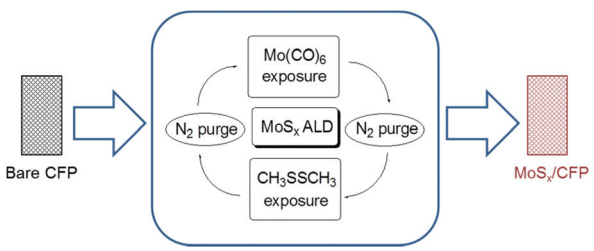

Fig. 1 Schematic diagram of the ALD process for preparing MoS_x/CFP catalysts.

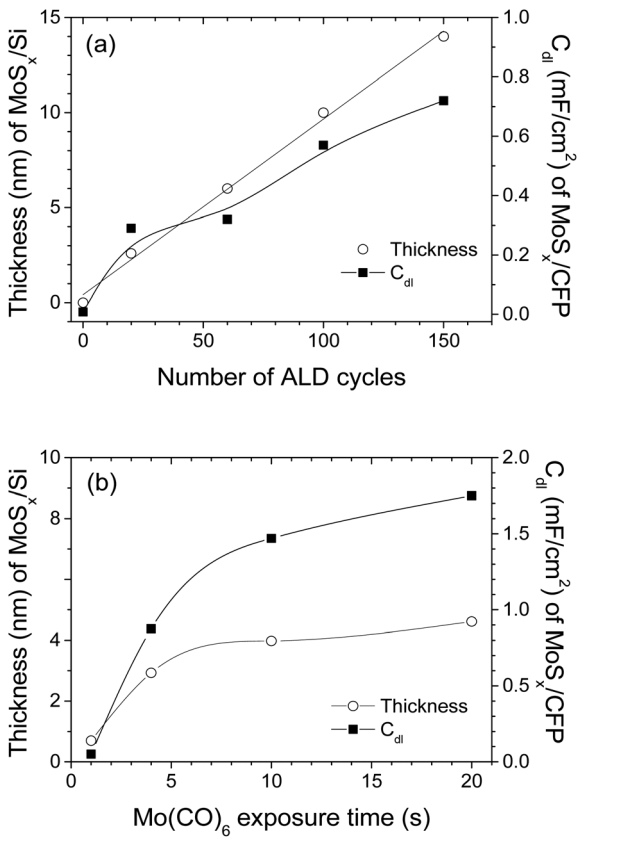

Fig. 2 Thickness (circles) and C_{dl} (squares) of MoS_x as functions of the number of ALD cycles (a) and the $Mo(CO)_6$ exposure time (b).

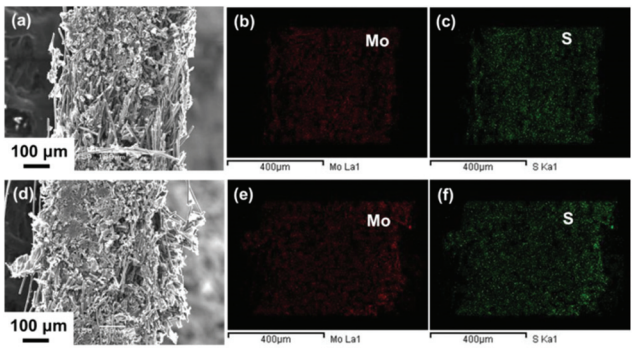

Fig. 3 Cross-sectional SEM images (a, d) of MoS_x/CFP and elemental mapping images of Mo and S. The ALD sequence of M (x)–P (90 s)–D (3 s)–P (60 s) was repeated at 100 °C for 50 cycles: (a–c) x = 1 s; (d–f) x = 20 s.

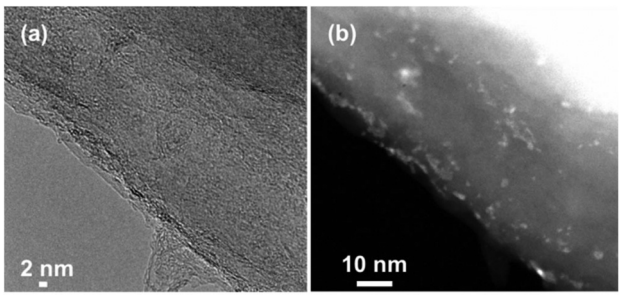

Fig. 4 HR-TEM (a) and STEM (b) images of MoS_x/CFP prepared by repeating the ALD sequence of M (x)–P (90 s)–D (1.5 s)–P (30 s) at 100 °C for 20 cycles.

4.2 mF cm^{-2}. It reveals that the ALD-MoS_x does not completely cover the entire surface of the CFP even at N_{ALD} = 150 cycles, due to its particle-like growth behavior (*vide infra*).

In Fig. 2b, the thickness of MoS_x on the Si saturates at long exposure times (x > 4 s) of $Mo(CO)_6$, which is a typical phenomenon of ALD indicating the self-limiting growth. Similarly, the C_{dl} of the MoS_x/CFP also increases with x, but the slope decreases when x > 10 s. A larger number of nuclei of MoS_x can nucleate on the surface of CFP by exposing the precursor for a longer time. However, the C_{dl} value (1.75 mF cm^{-2}) of the catalyst grown at the longest exposure time (at x = 20 s) is still smaller than 4.2 mF cm^{-2}. From eqn (1), the fractional surface coverage of MoS_x is roughly estimated to be θ = 0.42 at x = 20 s, assuming R_f = 1. It also supports the particle-like growth of MoS_x on the CFP.

Fig. 3 shows the cross-sectional and elemental mapping images of the MoS_x/CFP specimens by SEM-EDS. Due to the nanometer-scale size of the ALD-MoS_x catalyst, the appearances of the MoS_x/CFP in the SEM images are not significantly different from that of the bare CFP (Fig. S4†). Note that the particle-like structures shown in Fig. 3a and 3d are attributed to the carbonaceous cross-section of the CFP, which were formed when dividing the CFPs to prepare the specimens for the cross-sectional SEM images. However, in the cross-sectional elemental mapping images, it is clearly visible that the Mo and S atoms are uniformly distributed over the entire surface of the CFP regardless of the $Mo(CO)_6$ exposure time (x). Since the EDS peaks of Mo (Lα1, 2.235 keV) and S (Kα1, 2.249) are not clearly resolved but are slightly overlapped in the EDS analysis, it is difficult to determine the ratio of Mo/S across the cross-section of the CFP with the EDS analysis. However, the ratio of S to Mo is estimated to be 1.87 according to the XPS analysis on the MoS_x/CFP (see the paragraph for Fig. 7).

Generally, in an ALD process on nano-porous substrates with nanopores, a long exposure time of the precursor is required for the conformal and uniform growth of the film over the entire surface, because the film growth is limited by Knudsen-diffusion of the precursors.[23,28] Since the CFP substrate has micrometer-scale pores, the ALD growth of MoS_x on the CFP substrate is limited by the chemical adsorption of the precursors even at x = 1 s. However, it should be noted that the C_{dl} value (1.75 mF cm^{-2}) of the specimen prepared at the longest exposure time (x = 20 s) is significantly larger than that (0.05 mF cm^{-2}) of the other specimens (x = 1 s) as shown in Fig. 2b. These results imply that the sticking coefficient of $Mo(CO)_6$ on the CFP, defined as the ratio of the number of molecules adsorbed on a surface to the total number of the molecules striking the surface, is much smaller than the unity. In other words, only a small portion of the precursor molecules striking the surface can chemically adsorb on the surface of the graphitic carbon fiber. Consequently, the amount of MoS_x grown on the CFP depends on the exposure time of the precursors, because the sticking probability of the precursors becomes higher at a longer exposure time.

To investigate the morphology of MoS_x grown on the CFP substrate, the carbon fibers were detached from the specimen (N_{ALD} = 20), and the circumferential edge of the carbon fiber was imaged by high resolution (HR) TEM and scanning TEM (STEM) as shown in Fig. 4. In the HR-TEM image (Fig. 4a), the grown MoS_x is not clearly distinguished from the carbon fiber. However, the STEM image (Fig. 4b) obviously shows that MoS_x is grown like particles and randomly distributed on the surface of the carbon fiber. The bright particles are identified to be molybdenum sulfide by STEM-EDS (Fig. S5†). Note that the MoS_x particles are imaged with a brighter contrast than the carbon fiber in the Z-contrast. In Fig. 5, even if the number of ALD cycles increases to N_{ALD} = 50 cycles, the grown MoS_x is still particle-like. However, the size and the number of the MoS_x particles increase with N_{ALD}. In addition, the rectangular area in Fig. 5a was scanned by STEM-EDS to obtain elemental mapping images. The carbon atoms of the carbon fiber are uniformly detected in the whole area, but Mo and S atoms are observed only at the region where the bright particles are clearly visible in the STEM image. Therefore, it is confirmed that the grown particles are molybdenum sulfide.

The reason for the particle-like growth of MoS_x on CFP can be found in the intrinsic characteristics of the ALD process based on the chemical adsorption of precursors. Whether the ALD process will grow a thin film or result in particles strongly

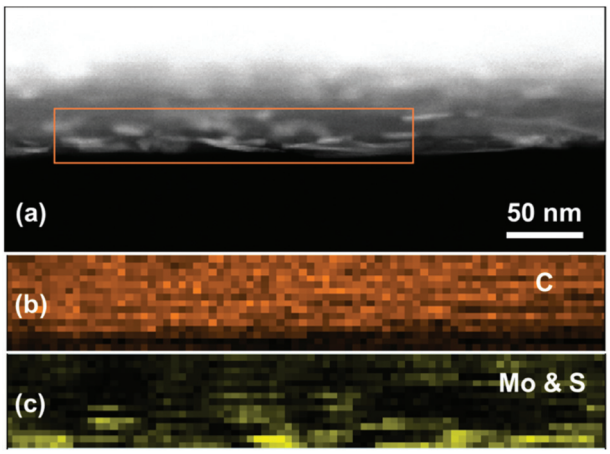

Fig. 5 STEM (a) and elemental mapping (b and c) images of molybdenum sulfide/CFP prepared by repeating the ALD sequence of M (20 s)–P (90 s)–D (3 s)–P (60 s) at 100 °C for 50 cycles.

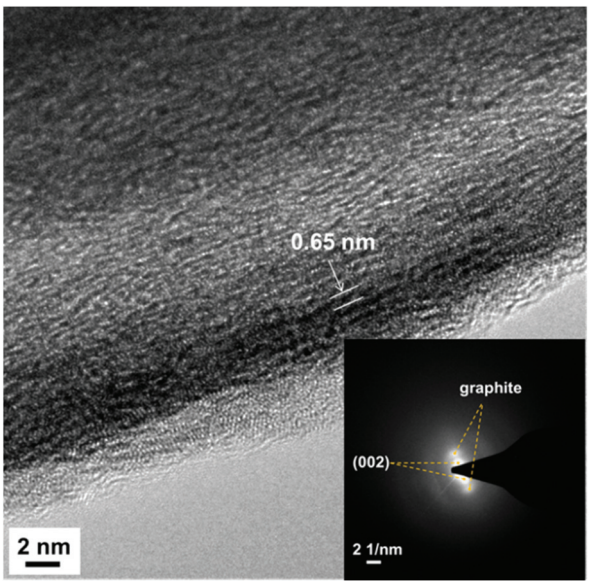

Fig. 6 HR-TEM image of MoS_x/CFP prepared by repeating the ALD sequence of M (4 s)–P (30 s)–D (1.5 s)–P (30 s) at 100 °C for 200 cycles. The inset shows the SAED pattern.

depends on the number of adsorption sites. According to our previous reports,[29,30] in the ALD of ZnO on carbon nanotubes, ZnO is not deposited in a thin film form, but grows in a particle form on the surface of carbon nanotubes. Because carbon nanotubes consist of sp^2 carbon atoms, the surface cannot provide a sufficient number of adsorption sites for the strong chemisorption of precursor molecules. Consequently, the nucleation for the growth may occur only on a certain type of adsorption site (*e.g.*, surface impurities and defects) to form the particles. Similarly, since the CFP substrate also has the graphitic structure, the particle-like growth of MoS_x may be attributed to the limited nucleation on the surface of the carbon fiber.

In the HR-TEM image of Fig. 6, the MoS_x grown on CFP for 200 ALD cycles has a mixed phase of amorphous and nanocrystalline structures, even though the growth temperature is only 100 °C. As denoted by arrows in Fig. 6, the interplanar spacing in the nano-crystallites is ~0.65 nm, which well agrees with that of the (002) planes of MoS_2. The selected area electron diffraction (SAED) pattern (inset image, the magnified image can be seen in Fig. S6†) also supports the presence of the nano-crystallites of MoS_2. The interplanar spacing of the (002) planes of MoS_2 is estimated to be 0.70 nm (±0.03) by taking the reciprocal of half the distance between the centrosymmetric spots in the inset figure. We also investigated the crystal structure of the catalyst by XRD analysis (Fig. S7†). A high intensity peak of the graphitic carbon of CFP is observed with a small peak of MoS_2 at 2Θ = 13.08°, which is attributed to the (002) basal planes of molybdenite. The interplanar spacing is calculated to be ~0.67 nm from the 2Θ value. The value is well consistent with the values of the interplanar spacing obtained by TEM images and SAED patterns. The presence of the nano-crystallites is also supported by the Raman spectroscopy observation, in which the characteristic in-plane (E^1_{2g}) and out-of-plane (A_{1g}) vibrational modes are occasionally observed with a weak intensity on the ALD-MoS_x/CFP (Fig. S8†). Considering that the same ALD process gives amorphous molybdenum sulfide films on SiO_2/Si and Au/Ti/Si substrates,[20,21] the presence of the nano-crystallites is unexpected. Recently, Kong and co-workers reported that crystalline MoS_2 layers could be grown on graphene at a low temperature of 400 °C *via* van der Waals epitaxy, compared to the high growth temperature (>800 °C) on the other substrates.[31] It is believed that the van der Waals interaction between MoS_2 and graphitic carbon may enable the growth of the nano-crystallites of MoS_2.

In Fig. 7, the chemical states of Mo and S are investigated on MoS_x/CFP by XPS. The binding energies were calibrated by using the carbon 1s peak at 284.8 eV. The ratio of S to Mo was estimated to be 1.87 from the peak intensities of S and Mo atoms on the surface. The characteristic binding energies of Mo^{4+} were observed at 231.8 and 228.7 eV for $3d_{3/2}$ and $3d_{5/2}$, respectively (Fig. 7a). However, similarly to the ALD-MoS_2 grown on Au,[21] the doublets of S^{2-} $2p_{1/2}$ and $2p_{3/2}$ peaks were not clearly resolved due to the presence of S_2^{2-} ions. Fig. 7b shows the deconvoluted spectra of the two doublets for both S^{2-} and S_2^{2-} ions. The binding energies of the $2p_{1/2}$ and $2p_{3/2}$ peaks appear at 163.2 and 162.1 eV for the S^{2-} ion, respectively. However, the doublets of the S_2^{2-} ion are located at 164.5 and 163.3 eV, respectively. The ratio of the divalent (S^{2-}) to monovalent (S_2^{2-}) sulfur ions is evaluated to be ~4.5 using the relative intensities of the deconvoluted doublets. Compared to the binding energy (229.1–229.2 eV) of $3d_{5/2}$ in the hydrothermal MoS_x/CFP of which the ratio of S^{2-}/S_2^{2-} is ranged from 0.3 to 0.7, the binding energy (228.7 eV) of Mo^{4+} $3d_{5/2}$ core electrons in the ALD-MoS_x/CFP is significantly red shifted.[19] The red shift of the binding energy of Mo^{4+} may be related to the ratio of S^{2-} to S_2^{2-} as shown in Fig. S9a.†

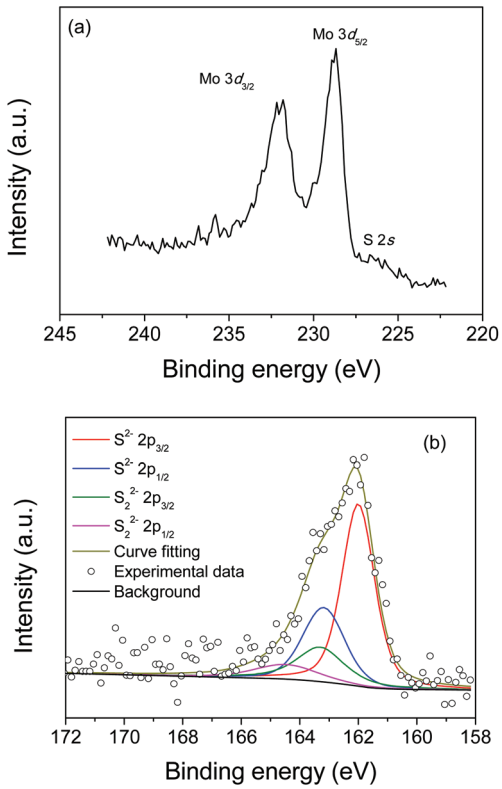

Fig. 7 XPS spectra of MoS_x on CFP: Mo 3d (a) and S 2p (b) peaks. The binding energies were calibrated with the adventitious carbon 1s peak (284.8 eV). The curve fitting was performed with two constraints: the intensity ratio (1 : 2) and the binding energy difference (1.18 eV) of S 2$p_{1/2}$ and 2$p_{3/2}$ for both S^{2-} and S_2^{2-} ions.

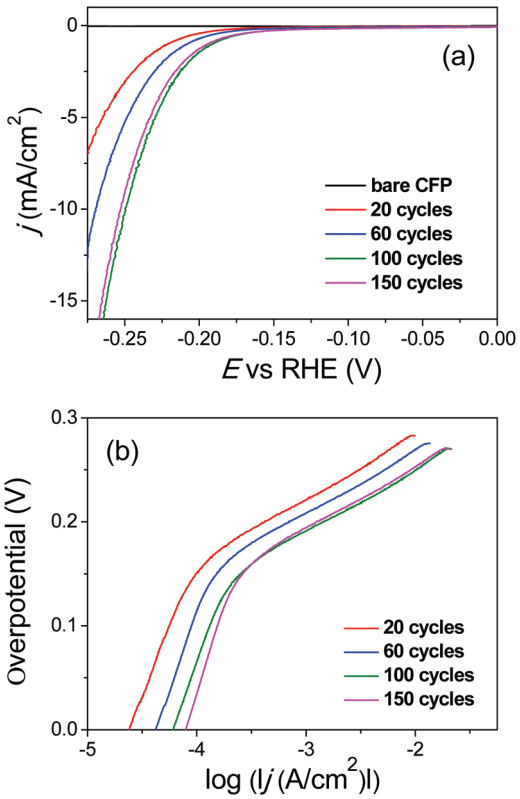

Fig. 8 HER polarization curves (a) and Tafel plots (b) of MoS_x/CFP catalysts prepared in the experimental set A.

In order to evaluate the electrochemical activity, which may depend on N_{ALD}, the MoS_x/CFP catalysts prepared in the experimental set A (N_{ALD} = 20, 60, 100, and 150 cycles) were used as a working electrode for hydrogen evolution in 0.5 M H_2SO_4 solution *via* the LSV method. Fig. 8a shows the polarization curves of each catalyst and bare CFP for the HER. As is well known, the bare CFP has no catalytic activity but the ALD-MoS_x catalysts show exponentially increasing cathodic current densities as the overpotential increases. In the previous report for the HER on the MoS_2/Au catalyst,[21] the overpotential required to reach 5 mA cm^{-2} is 254 mV. However, the MoS_x/CFP catalysts can generate twice the current density by applying the same overpotential, possibly due to its larger catalytically active surface area (A_c).

Eqn (2) may relate the electrochemically active surface area (A_e) to the geometric area (A_g) of the CFP with the roughness factor (R_f), fractional surface coverage (θ), and area multiplication factor (k),

$$A_e = kA_gR_f\theta \quad (2)$$

Because $R_f\theta = C_{dl}/C_{dl}^{\theta=1}$ in eqn (1), the A_e can be obtained from eqn (3),

$$A_e = kA_gC_{dl}/C_{dl}^{\theta=1} \quad (3)$$

where k = 70, A_g = 1 cm^2, and $C_{dl}^{\theta=1}$ = 4.2 mF cm^{-2} for our experiments. However, the A_e value may be different from the A_c value. Since the basal planes of crystalline MoS_2 are catalytically inert, and only the edge sites are active for the HER, the A_c value may be much smaller than the A_e value for the crystalline MoS_2. However, for the amorphous phase, the A_c and A_e values can be approximately equal owing to its isotropic nature. Here we define δ as a ratio of A_c to A_e, *i.e.*, $A_c = \delta A_e$. Therefore, the A_c value can be estimated by using eqn (4) as below

$$A_c = \delta kA_gC_{dl}/C_{dl}^{\theta=1} \quad (4)$$

where $\delta \sim 0$ for the basal plane of the perfectly crystalline MoS_2 parallel to the substrate and $\delta \sim 1$ for the amorphous molybdenum sulfide. Since the ALD-MoS_x catalyst has both amorphous and nano-crystalline phases as shown in Fig. 4–6, the δ value may be smaller than 1. Furthermore, as the ALD cycles are repeated after the nucleation of the nano-crystallites, the δ value may decrease due to the growth of the nano-crystallite. In Fig. 8a, the overpotential to reach 5 mA cm^{-2} on the 150-cycled catalyst is similar to or slightly larger than that on the 100-cycled MoS_x, which is attributed to the smaller δ value by the growth of the nano-crystallite.

Fig. 8b shows the Tafel plots of each catalyst. The overpotential (η) is plotted against the logarithm of the cathodic current density to determine the Tafel slope (b) and exchange

Table 1 Figures of merit for electrocatalytic activity of ALD-MoS_x /CFP catalysts (experimental set A)

N_{ALD}	Tafel slope (mV dec^{-1})	$j_0 = i_0/A_g$ (μA cm^{-2})	$j_0{}^* = i_0/A_e$ (μA cm^{-2})	TOF at 0.2 V *vs.* RHE (H_2 per s)
20	56.6	0.123	0.025	0.2–0.5
60	56.5	0.207	0.039	0.3–0.8
100	55.8	0.371	0.039	0.4–0.9
150	55.6	0.321	0.027	0.3–0.7

current density (j_0) using the Tafel equation: $\eta = a + b \log j$. The Tafel slopes of each catalyst are ranged in 55–57 mV dec^{-1}, which reveals that the HER mechanism on ALD-MoS_x catalysts are not significantly changed depending on N_{ALD}. Compared to the Tafel slope ($b \sim 47$ mV dec^{-1}) of amorphous MoS_x/Au grown by ALD in the previous work,[21] the Tafel slopes of the MoS_x/CFP are larger due to the presence of the nano-crystalline MoS_2, as listed in Table 1. The major pathway for the HER on the ALD-MoS_x/CFP may be the Volmer–Heyrovsky (VH̄) mechanism in which a primary discharging step (Volmer reaction) for hydrogen adsorption is followed by the rate-determining step (rds, the bar denotes the rds) of the electrochemical desorption of hydrogen gas (Heyrovsky reaction).[21,32] Even though the theoretical Tafel slope of the VH̄ mechanism is 40 mV dec^{-1}, the b value can become larger, when the crystalline phase is incorporated into the amorphous phase, as recently reported by Li and coworkers.[33]

Fig. 9a shows the polarization curves of the catalysts prepared by repeating 50 ALD cycles [M (x)–P (90 s)–D (3 s)–P (60 s)]. As the exposure time (x) of $Mo(CO)_6$ increases, the catalytic performance improves. Even for the catalyst prepared at x = 1s, which is not enough time to reach the complete coverage even on the Si substrate (open circles in Fig. 2b), the MoS_x catalyst is uniformly observed from the exterior to the interior surface of the CFP as shown in Fig. 3(a–c). Therefore, the improvement of the performance with a longer x is originated from the increase of the electrochemically-active surface area. Indeed, the cathodic current density at a specific overpotential (*e.g.*, η = 220 mV) shows the same tendency to the variation of C_{dl} as the exposure time increases (see Fig. S10†). The poor catalytic performance of the catalyst prepared at x = 1 s is due to the larger Tafel slope (77.9 mV dec^{-1}) than those (57–60 mV dec^{-1}) of the other catalysts as shown in Fig. 9b and Table 2.

The exchange current density is generally defined as $j_0 = i_0/A_g$, where i_0 is the cathodic current at η = 0. Tables 1 and 2 list the j_0 values of the ALD-MoS_x/CFP catalysts. Compared to the j_0 (0.02–0.03 μA cm^{-2}) of the ALD-MoS_2 on the flat Au/Si substrate in the previous report,[21] the ALD-MoS_x catalyst on the porous CFP exhibits one order of magnitude higher j_0 values. However, the direct comparison of the j_0 values is unfair between different types of substrates, because the A_e of the ALD-MoS_x/CFP is much larger than that of ALD-MoS_2/Au/Si. For a fair comparison, we introduce an effective exchange current density, which is defined as $j_0{}^* = i_0/A_e$, where A_e is obtained from eqn (1)–(3). The $j_0{}^*$ values of the MoS_x/CFP

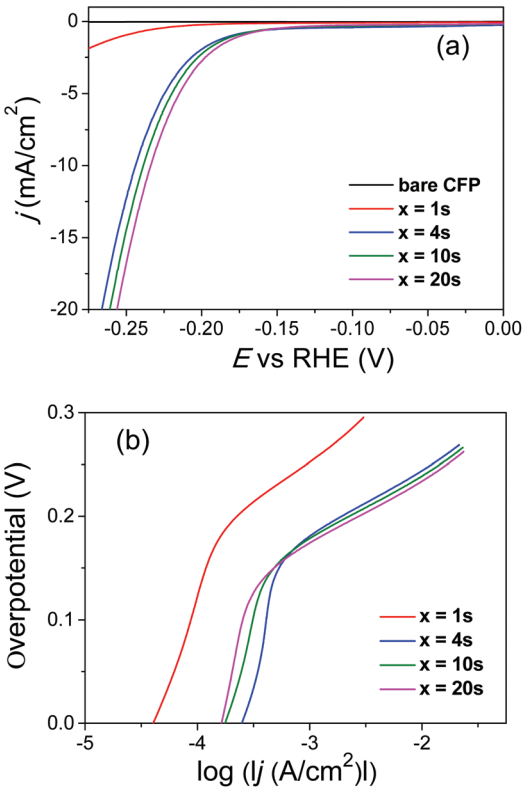

Fig. 9 HER polarization curves (a) and Tafel plots (b) of MoS_x/CFP catalysts prepared in the experimental set B: N_{ALD} = 50 cycles, M (x)–P (90 s)–D (3 s)–P (60 s).

Table 2 Figures of merit for the electrocatalytic activity of ALD-MoS_x /CFP catalysts (experimental set B)

x (s)	Tafel slope (mV dec^{-1})	$j_0 = i_0/A_g$ (μA cm^{-2})	$j_0{}^* = i_0/A_e$ (μA cm^{-2})	TOF at 0.2 V *vs.* RHE (H_2 per s)
1	77.9	0.566	[a]	[b]
4	59.9	0.880	0.059	0.3–0.8
10	57.6	0.756	0.031	0.2–0.6
20	57.3	0.883	0.030	0.2–0.6

[a] Not determined, because of its high uncertainty. [b] For x = 1 s, the overpotential of 0.2 V is out of the Tafel region.

catalysts are in the same order of magnitude as that (10^{-2} μA cm^{-2}) of the MoS_2/Au/Si as listed in Tables 1 and 2. Note that the $j_0{}^*$ value of the catalyst grown at x = 1 s in Table 2 cannot be determined because of its high uncertainty in the approximation of eqn (1).

One of the figures of merit for catalysis, by which the inherent catalytic activity of one catalyst is compared to that of another, is the turnover frequency (TOF) per active site. In the HER, the TOF represents the number of H_2 evolved on an active site for one second, which can be calculated by using eqn (5),

$$\mathrm{TOF} = jN_A/nFN \quad (5)$$

where n is the stoichiometric number of electrons consumed in the electrode reaction (n = 2 for the HER), and N is the number of active sites (*i.e.*, MoS_2) in the geometric area A_g (*i.e.*, 1 cm^2). N_A and F are Avogadro's number and the Faraday constant, respectively. Prior to estimating the TOF of the MoS_x/CFP catalyst, the number of active sites on the flat surface of MoS_2 should be determined for each polycrystalline and amorphous phase, because the ALD-MoS_x on the CFP has both amorphous and nano-crystalline phases. Recently, the number of active sites on the flat surfaces of MoS_2 has been approximately determined to be $N_{flat}^{polycrystalline} = 1.164 \times 10^{15}$ cm^{-2} for the polycrystalline phase and $N_{flat}^{amorphous} = 4.9 \times 10^{14}$ cm^{-2} for the amorphous phase.[17,21] Therefore, considering the area multiplication factor (k), roughness factor (R_f) and fractional surface coverage (θ), the real value of N falls between the two extreme cases as given in eqn (6).

$$N_{flat}^{amorphous} kR_f\theta < N < N_{flat}^{polycrystalline} kR_f\theta \quad (6)$$

Combining eqn (5) and (6), the TOF may be a value in the range of eqn (7).

$$\frac{jN_A}{nFN_{flat}^{polycrystalline} kR_f\theta} < \text{TOF} < \frac{jN_A}{nFN_{flat}^{amorphous} kR_f\theta} \quad (7)$$

Fig. 10 shows the per-site TOF of the representative MoS_x/CFP catalyst prepared in the experimental set A (N_{ALD} = 100 cycles). The TOF curve is drawn by using eqn (7) within the Tafel region to guarantee that the HER is controlled by electrode kinetics, and not by mass transfer limitations. The catalyst turns over the catalytic cycle with TOF = 0.4–0.9 H_2 per s at 0.2 V *vs.* RHE, which is lower than TOF = 1.45 H_2 per s on the amorphous ALD-MoS_2/Au/Si previously reported.[21] The lower TOF is attributed to the presence of the nano-crystalline MoS_2 in the mixed phase of MoS_x/CFP. It is well known that the amorphous phase is more active in the HER than the polycrystalline phase which has catalytically inactive basal planes.[8,33] Therefore, the TOF may be further improved by controlling the contribution of the amorphous MoS_x, and the edge sites of the crystalline MoS_2 in the mixed phase of the catalyst. It may be achieved by adjusting the growth temperature or destroying the basal (002) plane of MoS_2 after crystallizing the ALD-MoS_x/CFP at high temperature. The TOF values of other catalysts prepared in this work are also listed in Tables 1 and 2. Although the TOFs of ALD-MoS_x on CFP are lower than those of amorphous ALD-MoS_2 on Au, the TOFs are still slightly higher or similar to those of other amorphous MoS_x catalysts prepared by wet chemical synthesis (0.3 H_2 per s at 0.2 V), hydrothermal growth (0.32 H_2 per s at 0.2 V) or electrochemical deposition (0.8 H_2 per s at 0.22 V) methods.[16,17,19] The origin of the high TOFs on ALD-MoS_2/Au or ALD-MoS_x/CFP is still unclear. However, we can estimate that the high TOF is associated with the ratio of S^{2-}/S_2^{2-}, because they show strong correlation. In Fig. S9b,† as the ratio of S^{2-}/S_2^{2} increases, the TOF also increases.

The stability of the HER catalyst is another major concern for long-term operation. A cyclic voltammetry (CV) test was performed for 1000 cycles in a range of +0.1 V to −0.25 V *vs.* RHE at a scan rate of 50 mV s^{-1} in order to assess the stability of the MoS_x/CFP catalyst under acidic conditions (0.5 M H_2SO_4). In the previous report, the amorphous ALD-MoS_2 on Au had shown poor stability due to weak adhesion between MoS_2 and Au.[21] However, in Fig. 11, the MoS_x/CFP catalyst exhibits excellent stability as characterized by the negligible change in the polarization curves before and after 1000 CV cycles. We believe that the durable activity is attributed to two factors: the first is the strong adhesion between MoS_x and CFP by the van der Waals interaction, and the second is the mixed phase of the amorphous MoS_x and the nano-crystalline MoS_2 on the CFP. Another group has also reported that the incorporation of the nano-crystallite into the amorphous MoS_x could improve the stability of the molybdenum sulfide catalyst.[33]

Our ALD method enables the design and preparation of MoS_x electrocatalysts at an atomic scale. The major advantage of this ALD-grown catalyst is its excellent stability of the HER performance, which may be further improved by adjusting the crystallinity of the catalyst. The control of the crystallinity and

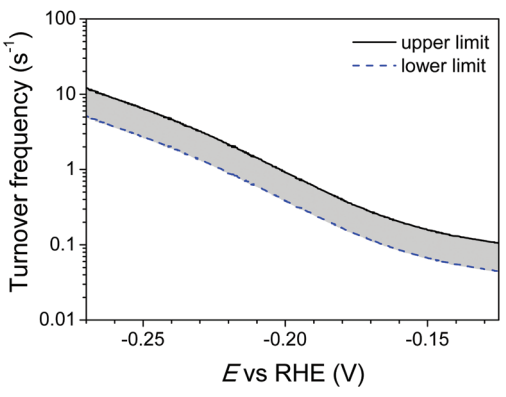

Fig. 10 Turnover frequency (TOF) of the MoS_x/CFP catalyst prepared in the experimental set A (N_{ALD} = 100 cycles). The solid and dotted lines are upper and lower limits, respectively, which are calculated by using eqn (7).

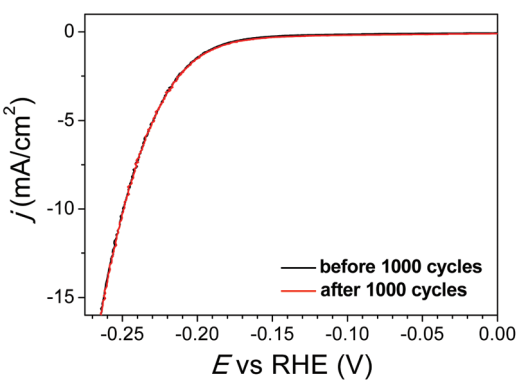

Fig. 11 Polarization curves of the MoS_x/CFP catalyst before and after 1000 CV cycles. The catalyst was prepared in the experimental set A (N_{ALD} = 100 cycles).

the active sites will be reported elsewhere, because it is out of the scope of this work.

Conclusions

We have grown MoS_x catalysts on CFP at 100 °C by ALD from molybdenum hexacarbonyl and dimethyl disulfide. The catalysts were formed on the porous CFP *via* particle-like growth behavior. The crystallographic structure of ALD-MoS_x on CFP is a mixture of amorphous and nano-crystalline phases. The Tafel slope of the representative MoS_x/CFP catalyst is around 56 mV dec^{-1}, indicating the Volmer–Heyrovsky mechanism. To compare the intrinsic activity of the ALD-MoS_x fairly, we have considered the area multiplication factor of CFP, roughness factor and fractional surface coverage of MoS_x on the CFP. Although the TOF of the MoS_x/CFP is slightly smaller than that of the amorphous ALD-MoS_2/Au due to the presence of the nano-crystalline MoS_2 in the MoS_x/CFP, it has exhibited excellent performance and stability.

Acknowledgements

This work was supported by Konkuk University in 2013. The authors thank M. K. Cho (Advanced Analysis Center, KIST) and Dr H. S. Baik (Analytical Research Division, KBSI) for XPS and TEM analyses, respectively.

Notes and references

1 J. A. Turner, *Science*, 2004, **305**, 972.
2 J. K. Norskov and C. H. Christensen, *Science*, 2006, **312**, 1322.
3 J. Greeley, T. F. Jaramillo, J. Bonde, I. B. Chorkendorff and J. K. Norskov, *Nat. Mater.*, 2006, **5**, 909.
4 C. G. Morales-guio, L. A. Stern and X. Hu, *Chem. Soc. Rev.*, 2014, **43**, 6555.
5 B. Hinnemann, P. G. Moses, J. Bonde, K. P. Jorgensen, J. H. Nielsen, S. Horch, I. Chorkendroff and J. K. Norskov, *J. Am. Chem. Soc.*, 2005, **127**, 5308.
6 M. R. Gao, Y. F. Xu, J. Jiang and S. H. Yu, *Chem. Soc. Rev.*, 2013, **42**, 2986.
7 H. Tributsch and J. C. Bennett, *J. Electroanal. Chem.*, 1977, **81**, 97.
8 T. F. Jaramillo, K. P. Jorgensen, J. Bonde, J. H. Nielsen, S. Horch and I. Chorkendorff, *Science*, 2007, **317**, 100.
9 Y. Li, H. Wang, W. L. Xie, Y. Liang, G. Hong and H. Dai, *J. Am. Chem. Soc.*, 2011, **133**, 7296.
10 Z. Chen, D. Cummins, B. N. Reinecke, E. Clark, M. K. Sunkara and T. F. Jaramillo, *Nano Lett.*, 2011, **11**, 4168.
11 J. Kibsgaard, Z. Chen, B. N. Reinecke and T. F. Jaramillo, *Nat. Mater.*, 2012, **11**, 963.
12 X. Bian, J. Zhu, L. Liao, M. D. Scanlon, P. Ge, C. Ji, H. H. Girault and B. Liu, *Electrochem. Commun.*, 2012, **22**, 128.
13 H. Wang, Z. Lu, S. Xu, D. Kong, J. J. Cha, G. Zheng, P. C. Hsu, K. Yan, D. Bradshaw, F. B. Prinz and Y. Cui, *Proc. Natl. Acad. Sci. U. S. A.*, 2013, **110**, 19701.
14 Y. Yan, B. Xia, Z. Xu and X. Wang, *ACS Catal.*, 2014, **4**, 1693.
15 M. R. Gao, M. K. Y. Chan and Y. Sun, *Nat. Commun.*, 2015, **6**, 7493.
16 D. Merki, S. Fierro, H. Vrubel and X. L. Hu, *Chem. Sci.*, 2011, **2**, 1262.
17 J. D. Benck, Z. Chen, L. Y. Kuritzky, A. J. Forman and T. F. Jaramillo, *ACS Catal.*, 2012, **2**, 1916.
18 Y. H. Chang, C. T. Lin, T. Y. Chen, C. L. Hsu, Y. H. Lee, W. Z. Zhang, K. H. Wei and L. J. Li, *Adv. Mater.*, 2013, **25**, 756.
19 B. Ranjith, S. K. Balasingam, S. Shin, Z. Jin, D. H. Kwon, Y. Jun and Y. S. Min, *Langmuir*, 2015, **31**, 5220.
20 Z. Jin, S. Shin, D. H. Kwon, S. J. Han and Y. S. Min, *Nanoscale*, 2014, **6**, 14453.
21 S. Shin, Z. Jin, D. H. Kwon, R. Bose and Y. S. Min, *Langmuir*, 2015, **31**, 1196.
22 B. J. O'Neill, D. H. K. Jackson, J. Lee, C. Canlas, P. C. Stair, C. L. Marshall, J. W. Elam, T. F. Kuech, J. A. Dumesic and G. W. Huber, *ACS Catal.*, 2015, **5**, 1804.
23 H. Y. Lee, C. J. An, S. J. Piao, D. Y. Ahn, M. T. Kim and Y. S. Min, *J. Phys. Chem. C*, 2010, **114**, 18601.
24 N. P. Dasgupta, C. Liu, S. Andrews, F. B. Prinz and P. Yang, *J. Am. Chem. Soc.*, 2013, **135**, 12932.
25 A. B. Laursen, P. Vesborg and I. Chorkendorff, *Chem. Commun.*, 2013, **49**, 4965.
26 Toray carbon fiber paper data sheet in http://fuelcellsetc.com/store/toray-paper-120.
27 Y. Yu, S. Y. Huang, Y. Li, S. Steinmann, W. Yang and L. Cao, *Nano Lett.*, 2014, **14**, 553.
28 Y. S. Min, E. J. Bae, K. S. Jeong, Y. J. Cho, J. H. Lee, W. B. Choi and G. S. Park, *Adv. Mater.*, 2003, **15**, 1019.
29 Y. S. Min, E. J. Bae, J. Song, J. B. Park, N. Park, U. J. Kim and W. Park, *Appl. Phys. Lett.*, 2007, **90**, 263104.
30 Y. S. Min, I. H. Lee, Y. H. Lee and C. S. Hwang, *CrystEngComm*, 2011, **13**, 3451.
31 Y. Shi, W. Zhou, A. Y. Lu, W. Fang, Y. H. Lee, A. L. Hsu, S. M. Kim, K. K. Kim, H. Y. Yang, L. J. Li, J. C. Idrobo and J. Kong, *Nano Lett.*, 2012, **12**, 2784.
32 J. O. M. Bockris and A. K. N. Reddy, *Modern Electrochemistry*, 1st edn, Plenum Press, New York, 1970, pp. 1242.
33 Y. Li, Y. Yu, Y. Huang, R. A. Nielsen, W. A. Goddard, Y. Li and L. Cao, *ACS Catal.*, 2015, **5**, 448.

Electronic Supplementary Information

Comprehensive study on atomic layer deposition of molybdenum sulfide for electrochemical hydrogen evolution

Do Hyun Kwon,[†a,b] Zhenyu Jin,[†a] Seokhee Shin,[a] Wook-Seong Lee,[b]* and Yo-Sep Min[a]*

[a]Department of Chemical Engineering, Konkuk University, 120 Neungdong-Ro, Gwangjin-Gu, Seoul 143-701, Korea.

[b]Electronic Materials Center, Korea Institute of Science and Technology, Seongbuk-Gu, Seoul 136-791, Korea.

† These authors equally contributed to this work.

*CORRESPONDING AUTHORS

Yo-Sep Min

Tel: +82-2-450-3197; fax: +82-2-458-3504; e-mail address: ysmin@konkuk.ac.kr

Wook-Seong Lee

e-mail: wsleemk@gmail.com

Ohmic potential drop (*iR*) correction

The ohmic drop correction was performed with the series resistances determined by the electrochemical impedance measurement. As shown in Fig. S1, all samples show similar series resistances ranged in 1 ~ 2 Ω. The *iR* correction for the LSV data was done with the series resistance by the equation of $\eta_{corr} = \eta_{exp} - iR$.

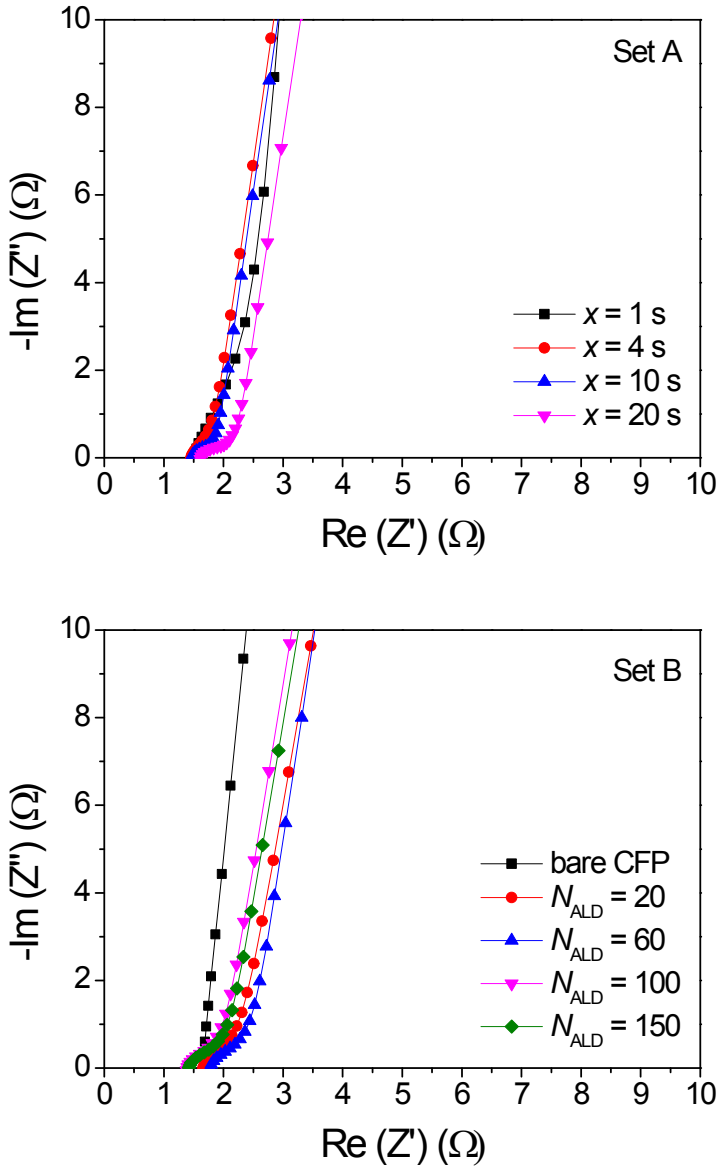

Fig. S1. Nyquist plots of bare CFP and MoS_x/CFP catalysts prepared in the experimental sets A and B.

Electrical Double Layer Capacitance

Generally, the electrochemically active surface area (A_e) is proportional to the double layer capacitance (C_{dl}). In order to calculate the electrical double layer capacitance, cyclic voltammetry was carried out in the range of +0.1 V ~ +0.2 V vs RHE with various scan rates of 20, 40, 60, 80, 100 mV/s. As shown in Fig. S2 and S3, the difference (Δj) between anodic and cathodic current densities were taken at 0.15 V vs RHE from the cyclic voltammograms, and then the values of Δj were plotted as a function of scan rate to obtain the slope, which correnspponds to twice the C_{dl} value. The similar data for the bare CFP can be found in the Supporting Information of Ref 19.

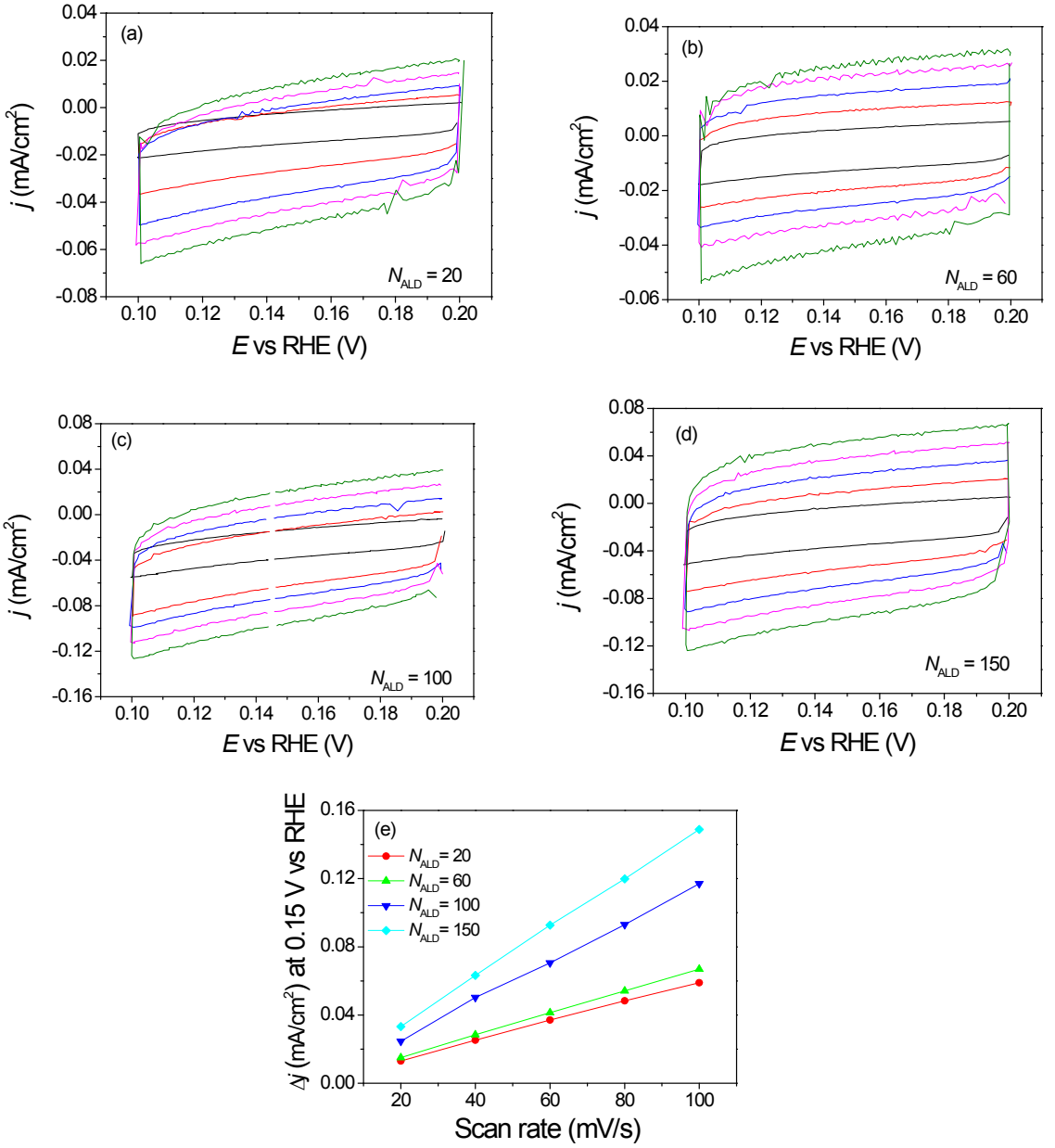

Fig. S2. (a-d) Cyclic voltammograms of MoS_x/CFP catalysts prepared in the experimental set A. (e) The plots of Δj – scan rate to obtain the C_{dl} values. The slope of the straight line is twice the C_{dl} value.

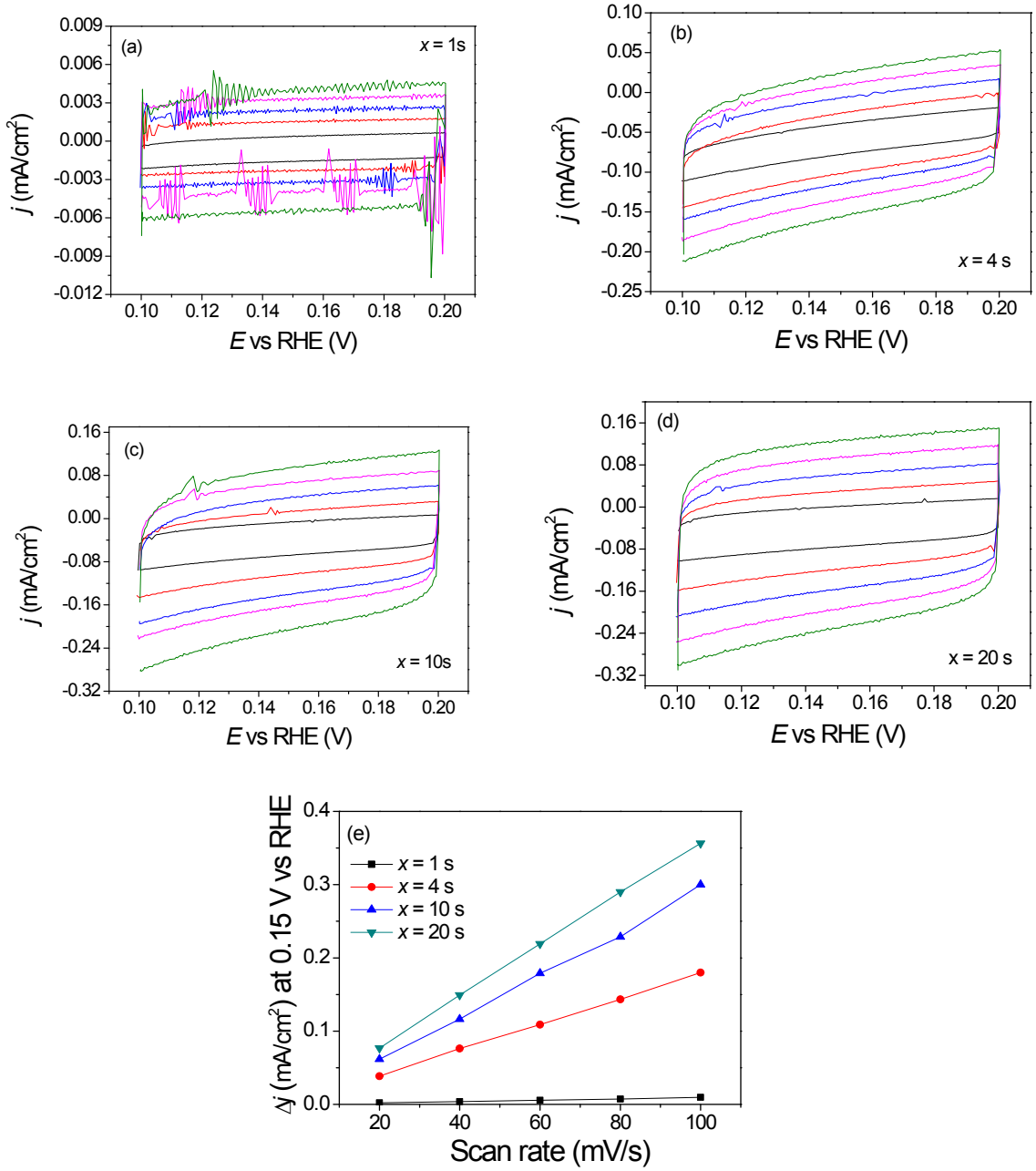

Fig. S3. (a-d) Cyclic voltammograms of MoS_x/CFP catalysts prepared in the experimental set B. (e) The plots of Δj – scan rate to obtain the C_{dl} values. The slope of the straight line is twice the C_{dl} value.

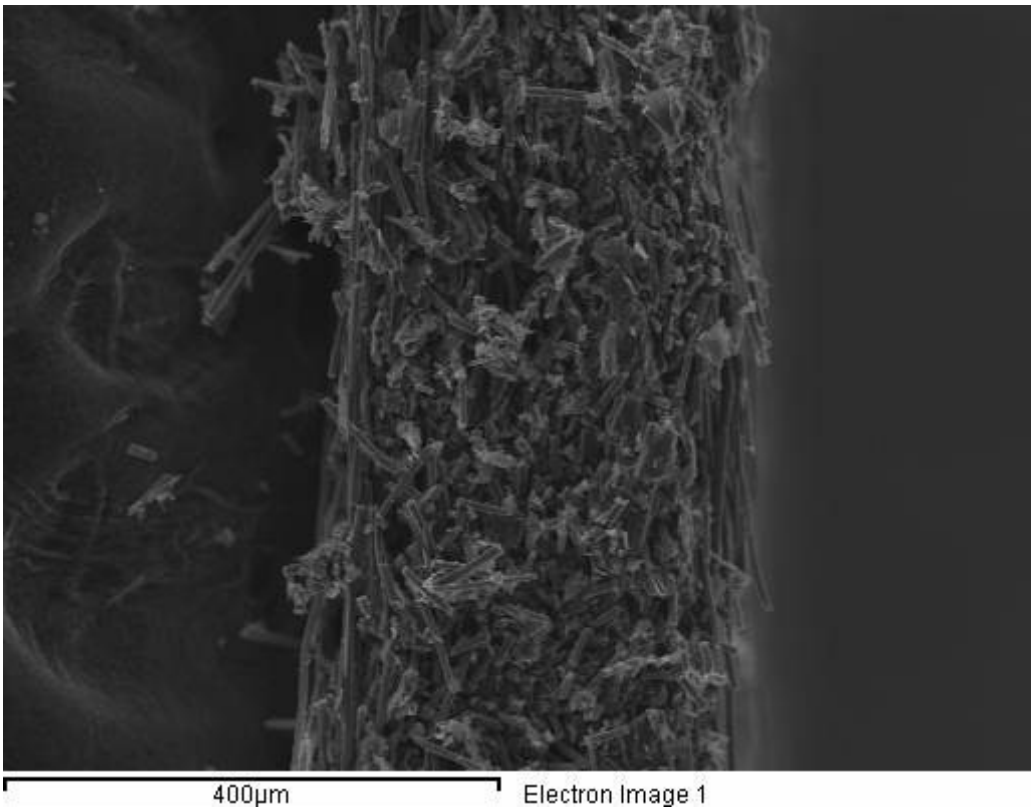

Fig. S4. Cross-sectional SEM image of bare CFP.

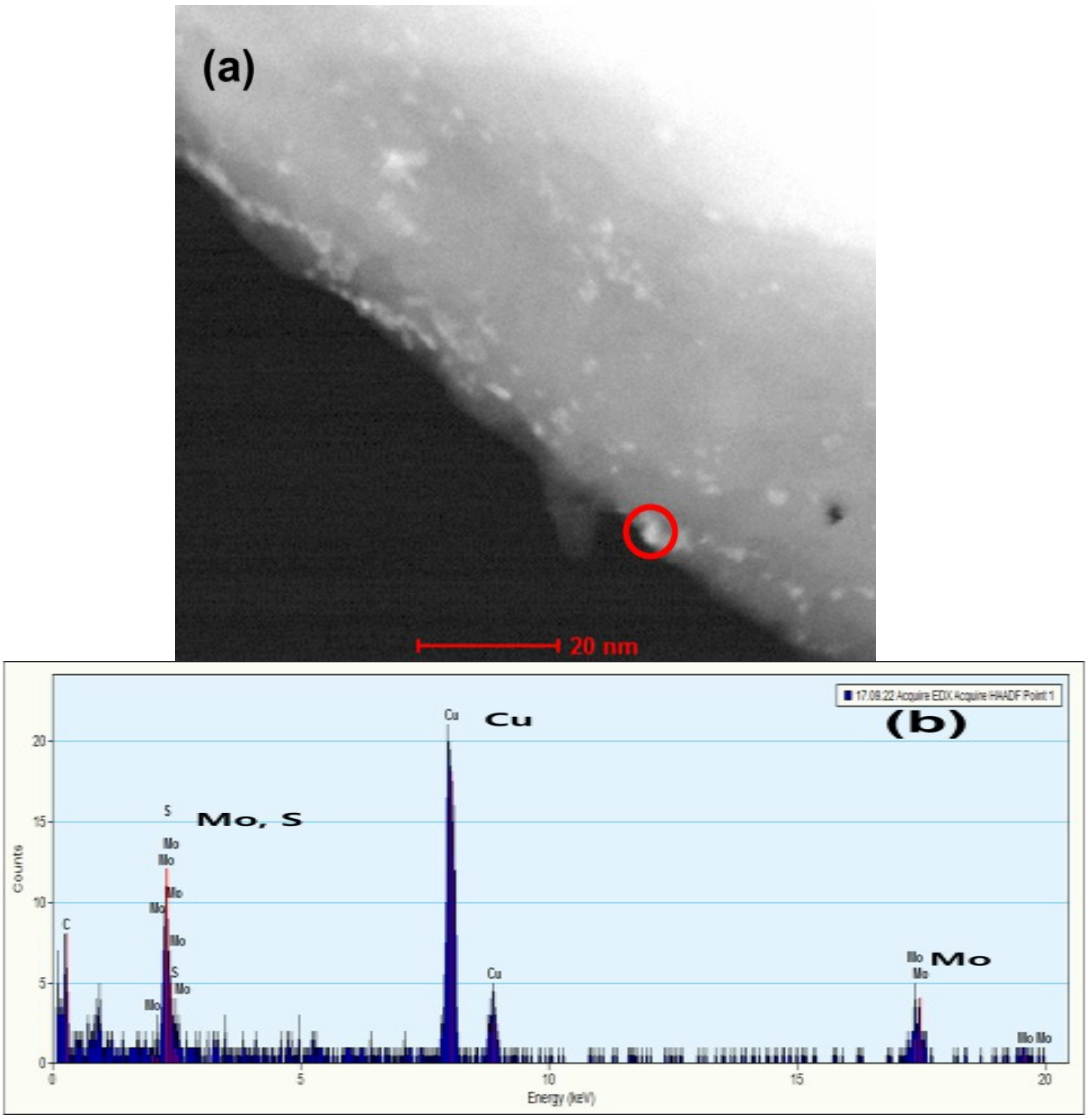

Fig. S5. (a) STEM images of MoS_x (20 cycles) on CFP. (b) EDS spectrum at the red circle in (a). Mo peak (Kα:17.441 keV, Lα: 2.293 keV); S peak (Kα: 2.307 keV); Cu peak (Kα: 8.040 keV, Lα: 0.930 keV) due to the Cu TEM grid.

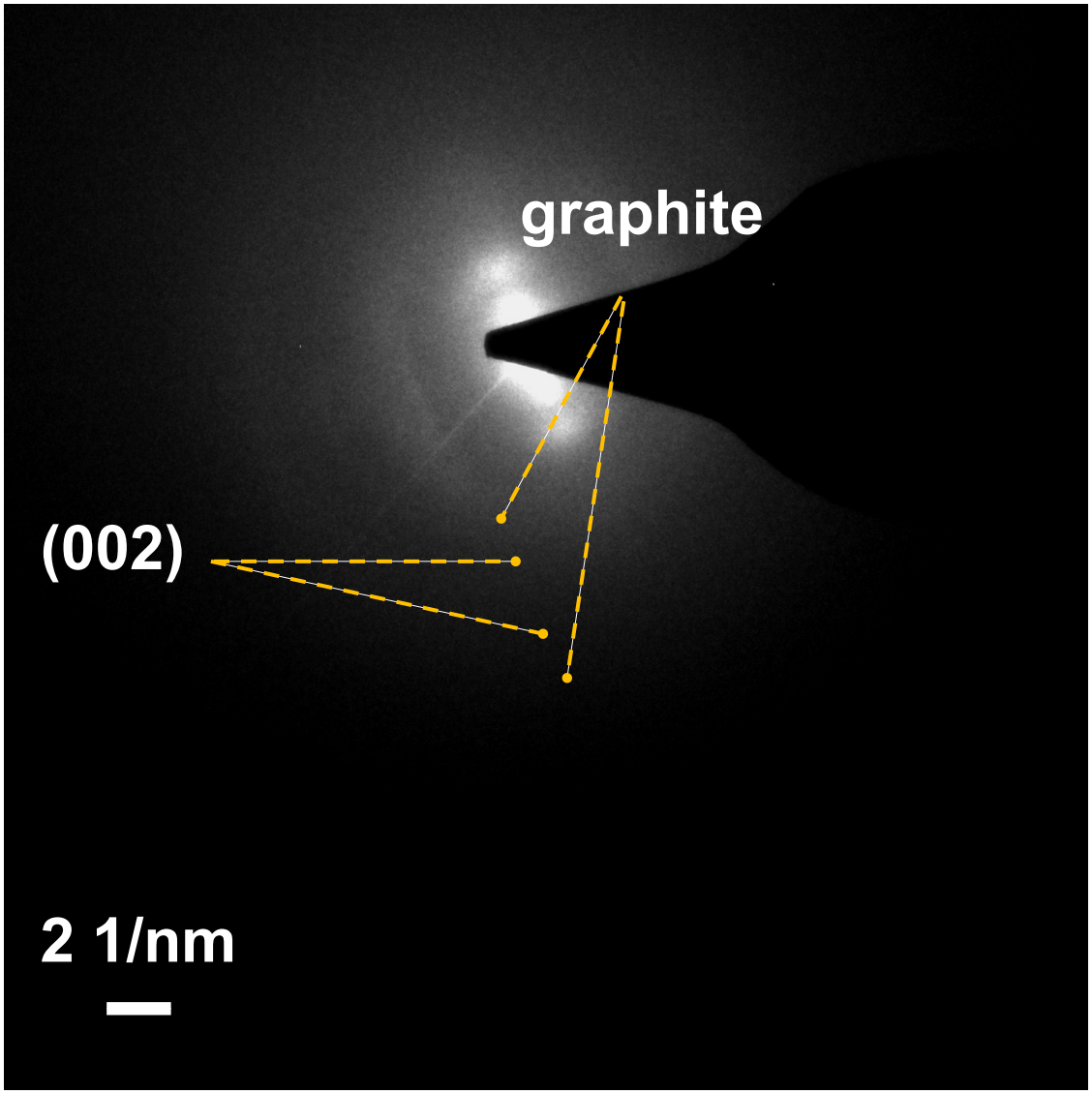

Fig. S6. The SAED pattern of MoS_x/CFP prepared by repeating the ALD sequence of M (4 s) – P (30 s) – D (1.5 s) – P (30 s) at 100 °C for 200 cycles.

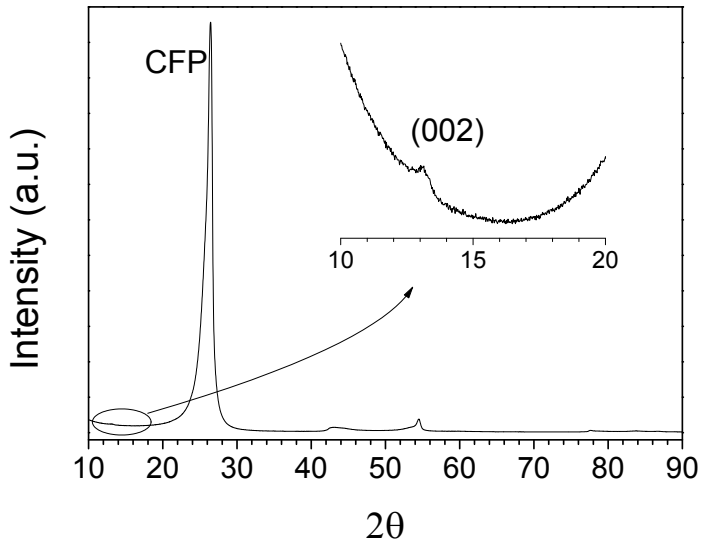

Fig. S7. XRD pattern of the MoS_x/CFP prepared by repeating the ALD sequence of M (4s) – P (30s) – D (1.5s) – P (30s) at 100 ^oC for 100 cycles. The inset figure was obtained by magnifying the XRD pattern in the range of $2\Theta = 10^o \sim 20^o$.

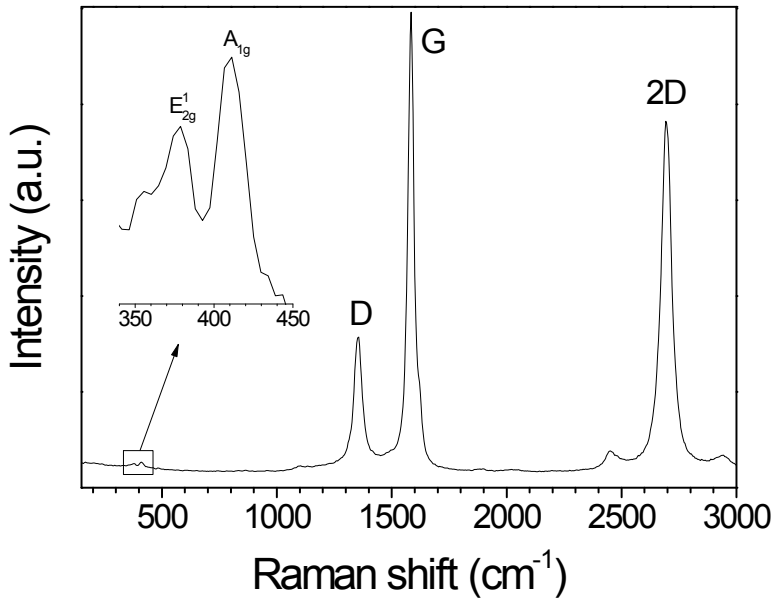

Fig. S8. Raman spectrum of ALD-MoS_x grown on CFP (532 nm laser excitation).

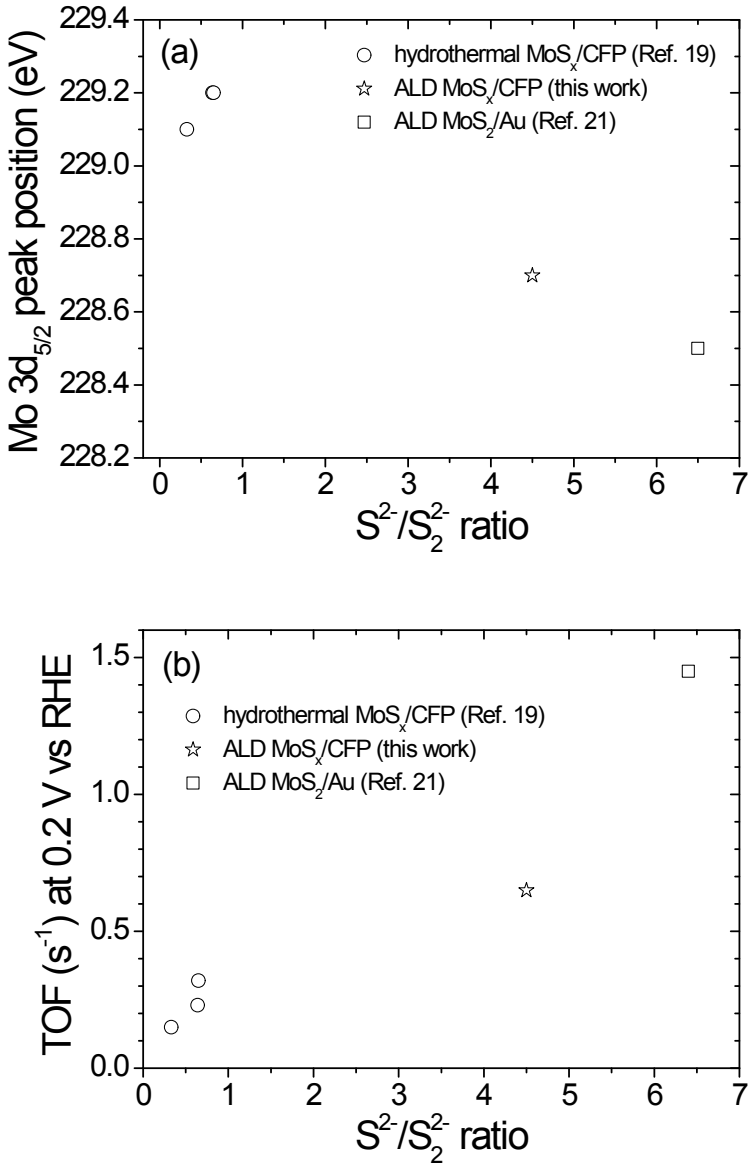

Fig. S9. Mo $3d_{5/2}$ binding energy (a) and turnover frequency (b) variations as a function of the ratio of S^{2-}/S_2^{2-}. In Fig. S9a, the binding energy was calibrated with the carbon 1s peak (284.8 eV) for this work and Ref. 19, and by using the Au $4f_{7/2}$ peak (84.0 eV) for Ref. 21. In Fig. S9b, the average TOF value at 0.2 V vs RHE was taken for the MoS_x/CFP because of the uncertainty from the mixed phase.

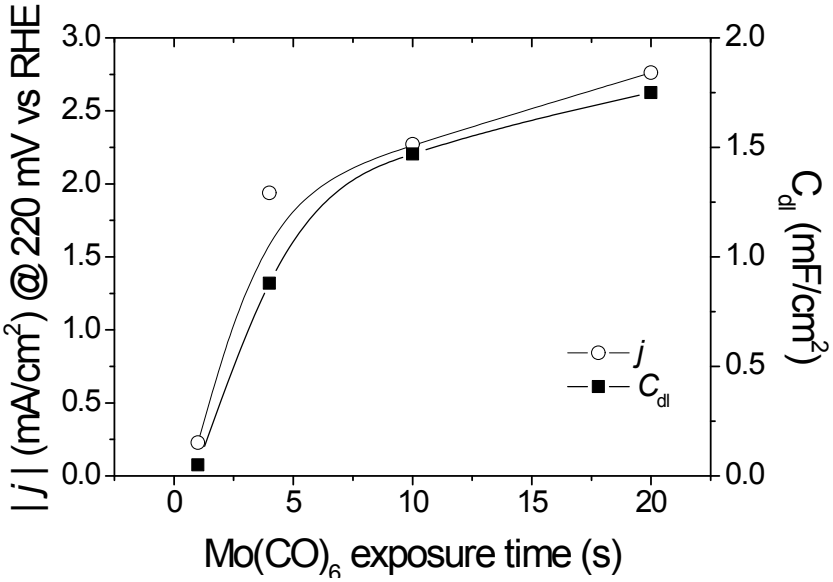

Fig. S10. Cathodic current density at 220 mV vs RHE (a) and electric double layer capacitance (b) variations as a function of the $Mo(CO)_6$ exposure time for the catalysts prepared in the experimental set B.